INTERNATIONAL JOURNAL FOR NUMERICAL METHODS IN FLUIDS
Int. J. Numer. Meth. Fluids 2002; **38**:1111–1131 (DOI: 10.1002/fld.263)

A class of higher order compact schemes for the unsteady two-dimensional convection–diffusion equation with variable convection coefficients

Jiten C. Kalita[1,*,†], D. C. Dalal[1] and Anoop K. Dass[2]

[1]*Department of Mathematics, Indian Institute of Technology, Guwahati 781039, India*
[2]*Department of Mech. Engineering, Indian Institute of Technology, Guwahati 781039, India*

SUMMARY

A class of higher order compact (HOC) schemes has been developed with weighted time discretization for the two-dimensional unsteady convection–diffusion equation with variable convection coefficients. The schemes are second or lower order accurate in time depending on the choice of the weighted average parameter μ and fourth order accurate in space. For $0.5 \leqslant \mu \leqslant 1$, the schemes are unconditionally stable. Unlike usual HOC schemes, these schemes are capable of using a grid aspect ratio other than unity. They efficiently capture both transient and steady solutions of linear and nonlinear convection–diffusion equations with Dirichlet as well as Neumann boundary condition. They are applied to one linear convection–diffusion problem and three flows of varying complexities governed by the two-dimensional incompressible Navier–Stokes equations. Results obtained are in excellent agreement with analytical and established numerical results. Overall the schemes are found to be robust, efficient and accurate. Copyright © 2002 John Wiley & Sons, Ltd.

KEY WORDS: 2-D; unsteady; convection–diffusion; HOC; N–S equations; accuracy

1. INTRODUCTION

The unsteady two-dimensional (2-D) convection–diffusion equation for a transport variable ϕ in some continuous domain with suitable boundary conditions can be written as

$$a\frac{\partial \phi}{\partial t} - \nabla^2 \phi + c(x, y, t)\frac{\partial \phi}{\partial x} + d(x, y, t)\frac{\partial \phi}{\partial y} = g(x, y, t) \tag{1}$$

where a is a constant, c and d are the convection coefficients, and g is a forcing function. In Equation (1), the magnitude of the convection coefficients determines the ratio of convection to diffusion and is sometimes referred to as the Reynolds number (Re). The equation becomes convection dominated for large Re's and diffusion dominated for small Re's. Most of the

*Correspondence to: J. C. Kalita, Department of Mathematics, Indian Institute of Technology, Guwahati, North Guwahati, Guwahati 781039, India.
†E-mail: jiten@iitg.ernet.in

Received 3 May 2000
Revised 26 June 2001

Copyright © 2002 John Wiley & Sons, Ltd.

unsteady 2-D flows are expressed in this form. It represents the convection–diffusion of many fluid variables such as mass, heat, energy, vorticity etc. With proper choice of a, c, d and g, it can also be used to represent the complete Navier–Stokes (N–S) equations.

Till about two decades ago, second order accuracy was considered to be sufficient for most CFD applications. In particular, the central difference and upwind schemes have been the most popular ones because of their straightforwardness in application. Though for problems having well-behaved solutions, they often yield quite good results on reasonable meshes, the solution may be of poor quality for convection dominated flows if the mesh is not sufficiently refined. Again, higher order discretization is generally associated with non-compact stencils which increase the band-width of the resultant coefficient matrix. Both mesh refinement and increased matrix band-width invariably lead to a large number of arithmetic operations. Thus, neither a lower order accurate method on a fine mesh nor a higher order accurate one on a non-compact stencil seems to be computationally cost-effective. This is where higher order compact (HOC) finite difference methods become important. A compact finite difference scheme is one which utilizes grid points located only directly adjacent to the node about which differences are taken. In addition, if the scheme has an accuracy greater than two, it is termed an HOC method. The higher order accuracy of the HOC methods combined with the compactness of the difference stencils yields highly accurate numerical solutions on relatively coarser grids with greater computational efficiency. Such methods can be obtained through different mechanisms. One of them is to use the original differential equation to replace the derivatives appearing in the leading truncation error (TE) terms of the standard central difference approximation. This idea was first attempted by Lax and Wendroff [1–3] on the unsteady hyperbolic partial differential equations (PDEs). They used the original PDE to replace the second order time derivative in a Taylor series expansion, thus raising the time accuracy of the scheme from order one to two. The spatial implementation of this temporal Lax–Wedroff idea was first proposed by Mackinnon and Carey [4]. Similar research was carried out by Mackinnon and Johnson [5] in order to develop schemes for steady-state convection–diffusion equations. Spotz and Carey [6] then extended this $O(h^4)$ scheme (h is the grid spacing) to the steady-state stream-function vorticity ($\psi - \omega$) formulation of the N–S equations.

There have been attempts to develop HOC schemes for transient problems as well. Several explicit or partially implicit higher order schemes were developed for the unsteady incompressible N–S equations by Hirsh [7] and Rai and Moin [8], and for compressible N–S equations by Lele [9]. Abarbanel and Kumar [10], at about the same time, proposed some explicit schemes based on the HOC approach for the Euler equations. These schemes are spatially fourth and temporally second order accurate. Recently a second order time accurate explicit scheme for 2-D advection dominated flows has been presented by Balzano [11]. Explicit schemes, though very easy to implement, have a severe stability limit to the time step [1–3].

On the other hand, implicit schemes can be applied to obtain a time-accurate solution of an inherently unsteady flow or time marching steady-state solution with a larger time step. Several higher order implicit schemes for the one dimensional (1-D) time dependent convection–diffusion problems were developed by Noye and Tan [12]. Later on, they also developed a nine-point scheme of third order spatial and second order temporal accuracy for the 2-D convection–diffusion equations with constant coefficients [13]. The 2-D fourth order accurate nine-point HOC scheme proposed in Reference [6] was extended by Spotz to solve the unsteady 1-D convection–diffusion and 2-D diffusion equations [14]. Few other schemes that have been developed for the unsteady 2-D N–S equations are the implicit higher order

Copyright © 2002 John Wiley & Sons, Ltd.

accurate schemes of Strikwerda [15], the upwind compact scheme of Yanwen *et al.* [16] and the implicit weighted essentially non-oscillatory scheme of Chen *et al.* [17]. Some of these schemes (for example, Reference [15]), however, could not adequately capture the high Reynolds number regime of incompressible viscous flows.

The present work proposes a class of implicit HOC schemes for the 2-D unsteady convection–diffusion in line with the steady-state scheme of Reference [5]. In the process it also removes, for the first time, the restriction of usual HOC schemes [5, 6] of having to use a grid aspect ratio of unity. The schemes accommodate Dirichlet as well as Neumann boundary condition easily. They solve very accurately and efficiently the unsteady 2-D convection–diffusion problems including 2-D incompressible N–S equations. One important factor is that determines the merit of a scheme for transient problems is the time-wise accuracy [2, 18] and one of the proposed schemes is temporally second and spatially fourth order accurate. To test the robustness, accuracy and efficiency of the schemes, they are applied to four pertinent test cases for which numerical and/or analytical results are available. The first one serves as a perfect example to illustrate inherent features of the schemes like diffusion and anti-diffusion and their suppression. It is evident from the next two test cases that the proposed schemes accurately capture the transient flow of problems governed by the 2-D incompressible N–S equations even for a Reynolds number as high as 10 000. Also being implicit in nature, they capture the steady-state time marching solutions very efficiently as can be seen from the last case. Grid independence studies and error analysis have been carried out wherever necessary. Comparison with analytical and established numerical results shows excellent agreement.

The paper has been arranged in five sections. Section 2 deals with discretization and issues related to it, Section 3 with stability analysis, Section 4 with the numerical test cases and finally, Section 5 summarizes the whole work.

2. DISCRETIZATION AND RELATED ISSUES

At the outset of this section, we briefly discuss the development of HOC formulation for the steady-state form of Equation (1), which is obtained when ϕ, c, d and g are independent of t. Under these conditions, Equation (1) becomes

$$-\nabla^2\phi + c(x,y)\frac{\partial\phi}{\partial x} + d(x,y)\frac{\partial\phi}{\partial y} = g(x,y) \tag{2}$$

Assuming the problem domain to be rectangular and constructing on it a uniform rectangular mesh of steps h and k in the x- and y-directions respectively, the standard central difference approximation to Equation (2) at the (i,j)th node is given by

$$-\delta_x^2\phi_{ij} - \delta_y^2\phi_{ij} + c\delta_x\phi_{ij} + d\delta_y\phi_{ij} - \tau_{ij} = g_{ij} \tag{3}$$

where ϕ_{ij} denotes $\phi(x_i, y_j)$; δ_x, δ_x^2 and δ_y, δ_y^2 are the first and second order central difference operators along x- and y-directions respectively. The truncation error τ_{ij} is given by

$$\tau_{ij} = \left[\frac{h^2}{12}\left(2c\frac{\partial^3\phi}{\partial x^3} - \frac{\partial^4\phi}{\partial x^4}\right) + \frac{k^2}{12}\left(2d\frac{\partial^3\phi}{\partial y^3} - \frac{\partial^4\phi}{\partial y^4}\right)\right]_{ij} + O(h^4, k^4) \tag{4}$$

Copyright © 2002 John Wiley & Sons, Ltd.

To obtain a fourth order compact formulation for Equation (2), each of the derivatives of the leading term of Equation (4) are compactly approximated [5, 6] to $O(h^2, k^2)$. In order to accomplish this, the original PDE of Equation (2) is treated as an auxiliary relation that can be differentiated to yield expressions for higher derivatives. For example the derivative in the first term on the right hand side of Equation (4) can be written as

$$\left.\frac{\partial^3\phi}{\partial x^3}\right|_{ij} = \left[-\frac{\partial^3\phi}{\partial x\partial y^2} + c\,\frac{\partial^4\phi}{\partial x^2} + \frac{\partial c}{\partial x}\,\frac{\partial\phi}{\partial x} + d\,\frac{\partial^2\phi}{\partial x\partial y} + \frac{\partial d}{\partial x}\,\frac{\partial\phi}{\partial y} - \frac{\partial g}{\partial x}\right]_{ij}$$

$$= [-\delta_x\delta_y^2 + c_{ij}\delta_x^2 + \delta_x c_{ij}\delta_x + d_{ij}\delta_x\delta_y + \delta_x d_{ij}\delta_y]\phi_{ij} - \delta_x g_{ij}$$

$$+ O(h^2, k^2) \tag{5}$$

Similar approximations can be constructed for the other derivatives as well. For such compact schemes, $[(\partial^n\phi)/(\partial x^n)]$ or $[(\partial^n\phi)/(\partial y^n)]$ is generally replaced by a combination of terms involving products of $[(\partial^{p+q}\phi)/(\partial x^p\partial y^q)]$ and the convection coefficients or their derivatives with $p + q \leqslant n$. For a fourth order accurate scheme, $n \leqslant 4$ and compactness is maintained keeping $p, q \leqslant 2$. Thus replacing the derivatives in Equation (4) with approximations such as Equation (5) and subsequent substitution for τ_{ij} in Equation (3) yields the $O(h^4, k^4)$ approximation for Equation (2) on a nine-point stencil as

$$-\alpha_{ij}\delta_x^2\phi_{ij} - \beta_{ij}\delta_y^2\phi_{ij} + C_{ij}\delta_x\phi_{ij} + D_{ij}\delta_y\phi_{ij}$$

$$-\frac{h^2+k^2}{12}[\delta_x^2\delta_y^2 - c_{ij}\delta_x\delta_y^2 - d_{ij}\delta_x^2\delta_y - \gamma_{ij}\delta_x\delta_y]\phi_{ij} = G_{ij} \tag{6}$$

where the coefficients α_{ij}, β_{ij}, γ_{ij}, C_{ij}, D_{ij} and G_{ij} are as follows:

$$\alpha_{ij} = 1 + \frac{h^2}{12}(c_{ij}^2 - 2\delta_x c_{ij}) \tag{7}$$

$$\beta_{ij} = 1 + \frac{k^2}{12}(d_{ij}^2 - 2\delta_y d_{ij}) \tag{8}$$

$$\gamma_{ij} = \frac{2}{h^2+k^2}(h^2\delta_x d_{ij} + k^2\delta_y c_{ij}) - c_{ij}d_{ij} \tag{9}$$

$$C_{ij} = \left[1 + \frac{h^2}{12}(\delta_x^2 - c_{ij}\delta_x) + \frac{k^2}{12}(\delta_y^2 - d_{ij}\delta_y)\right]c_{ij} \tag{10}$$

$$D_{ij} = \left[1 + \frac{h^2}{12}(\delta_x^2 - c_{ij}\delta_x) + \frac{k^2}{12}(\delta_y^2 - d_{ij}\delta_y)\right]d_{ij} \tag{11}$$

$$G_{ij} = \left[1 + \frac{h^2}{12}(\delta_x^2 - c_{ij}\delta_x) + \frac{k^2}{12}(\delta_y^2 - d_{ij}\delta_y)\right]g_{ij} \tag{12}$$

Copyright © 2002 John Wiley & Sons, Ltd.

Here, it is assumed that the convection coefficients c, d and the forcing function g are sufficiently smooth so that they are at least twice differentiable, and either the analytical expressions or discrete approximations of them together with their derivatives are known *a priori.*

For an unsteady case, the equation with variable coefficients will be similar to Equation (2), but the coefficients c and d are functions of x, y and t, and the expression on the right hand side becomes $g(x, y, t) - a[(\partial\phi)/(\partial t)]$. Using forward difference for $[(\partial\phi)/(\partial t)]$ with a time step Δt, we approximate the unsteady equation with the help of Equation (6) as

$$\begin{aligned} & a\left[1+\overbrace{\frac{h^2}{12}(\delta_x^2-c_{ij}\delta_x)+\frac{k^2}{12}(\delta_y^2-d_{ij}\delta_y)}\right]\delta_t^+\phi_{ij}^n \\ & -\alpha_{ij}\delta_x^2\phi_{ij}^n-\beta_{ij}\delta_y^2\phi_{ij}^n+C_{ij}\delta_x\phi_{ij}^n+D_{ij}\delta_y\phi_{ij}^n \\ & -\frac{h^2+k^2}{12}[\delta_x^2\delta_y^2-c_{ij}\delta_x\delta_y^2-d_{ij}\delta_x^2\delta_y-\gamma_{ij}\delta_x\delta_y]\phi_{ij}^n=G_{ij}^n \end{aligned} \tag{13}$$

where δ^+ denotes the forward difference operator and the superscript n stands for the time level. Equation (13) can be rewritten as

$$\sum_{k_1=-1}^{1}\sum_{k_2=-1}^{1} w_{i+k_1,j+k_2}\phi_{i+k_1,j+k_2}^{n+1}=\sum_{k_1=-1}^{1}\sum_{k_2=-1}^{1} w'_{i+k_1,j+k_2}\phi_{i+k_1,j+k_2}^{n}+12G_{ij} \tag{14}$$

where $w_{i+k_1,j+k_2}=q_{i+k_1,j+k_2}$, $w'_{i+k_1,j+k_2}=12\,p_{i+k_1,j+k_2}+q_{i+k_1,j+k_2}$, with $\lambda_1=(\Delta t/h^2)$, $\lambda_2=[(\Delta t)/(k^2)]$ and

$$\begin{aligned} p_{i-1,j-1} &= \frac{\lambda_1+\lambda_2}{2}\left(-\frac{1}{6}-\frac{c_{ij}h}{12}-\frac{d_{ij}k}{12}+\frac{\gamma_{ij}hk}{24}\right), & q_{i-1,j-1}&=0 \\ p_{i,j-1} &= -\lambda_2\beta_{ij}-\frac{\lambda_2 D_{ij}k}{2}+\frac{\lambda_1+\lambda_2}{6}+\frac{d_{ij}k(\lambda_1+\lambda_2)}{12}, & q_{i,j-1}&=a\left(1+\frac{d_{ij}k}{2}\right) \\ p_{i+1,j-1} &= \frac{\lambda_1+\lambda_2}{2}\left(-\frac{1}{6}+\frac{c_{ij}h}{12}-\frac{d_{ij}k}{12}-\frac{\gamma_{ij}hk}{24}\right), & q_{i+1,j-1}&=0 \\ p_{i-1,j} &= -\lambda_1\alpha_{ij}-\frac{\lambda_1 C_{ij}h}{2}+\frac{\lambda_1+\lambda_2}{6}+\frac{c_{ij}h(\lambda_1+\lambda_2)}{12}, & q_{i-1,j}&=a\left(1+\frac{c_{ij}h}{2}\right) \\ p_{ij} &= 2\lambda_1\alpha_{ij}+2\lambda_2\beta_{ij}-\frac{\lambda_1+\lambda_2}{3}, & q_{ij}&=8a \\ p_{i+1,j} &= -\lambda_1\alpha_{ij}+\frac{\lambda_1 C_{ij}h}{2}+\frac{\lambda_1+\lambda_2}{6}-\frac{c_{ij}h(\lambda_1+\lambda_2)}{12}, & q_{i+1,j}&=a\left(1-\frac{c_{ij}h}{2}\right) \\ p_{i-1,j+1} &= \frac{\lambda_1+\lambda_2}{2}\left(-\frac{1}{6}-\frac{c_{ij}h}{12}+\frac{d_{ij}k}{12}-\frac{\gamma_{ij}hk}{24}\right), & q_{i-1,j+1}&=0 \end{aligned}$$

Copyright © 2002 John Wiley & Sons, Ltd.

$$p_{i,j+1} = -\lambda_2\beta_{ij} + \frac{\lambda_2 D_{ij}k}{2} + \frac{\lambda_1+\lambda_2}{6} - \frac{d_{ij}k(\lambda_1+\lambda_2)}{12}, \quad q_{i,j+1} = a\left(1 - \frac{d_{ij}k}{2}\right)$$

$$p_{i+1,j+1} = \frac{\lambda_1+\lambda_2}{2}\left(-\frac{1}{6} + \frac{c_{ij}h}{12} + \frac{d_{ij}k}{12} + \frac{\gamma_{ij}hk}{24}\right), \qquad q_{i+1,j+1} = 0$$

A weighted average parameter μ is now introduced through the use of the forward time approximation of $[(\partial\phi)/(\partial t)]$ such that $t_\mu = (1-\mu)t^n + \mu t^{n+1}$ for $0 \leqslant \mu \leqslant 1$. Varying μ provides a class of integrators; for example, forward Euler for $\mu = 0$, backward Euler for $\mu = 1$ and Crank–Nicholson for $\mu = 0.5$. Consequently, the coefficients $w_{i+k_1,j+k_2}$ and $w'_{i+k_1,j+k_2}$ in Equation (14) can be written as $w_{i+k_1,j+k_2} = 12\mu p_{i+k_1,j+k_2} + q_{i+k_1,j+k_2}$ and $w'_{i+k_1,j+k_2} = 12(\mu - 1)p_{i+k_1,j+k_2} + q_{i+k_1,j+k_2}$ respectively, and G_{ij}^n on the right hand side of Equation (14) takes the form $\mu G_{ij}^{n+1} + (1-\mu)G_{ij}^n$. With these replacements, Equation (14) becomes the HOC finite-difference approximation for the unsteady 2-D convection–diffusion equation with fourth order spatial accuracy. All the schemes arising in this way are implicit because of the operator under the brace in Equation (13). The accuracy of the schemes is $O((\Delta t)^s, h^4, k^4)$, with $s \leqslant 2$. Again, it should be noted that for $\mu = 0$, the difference stencil requires nine points in the nth and five points in the $(n+1)$th time level resulting in what may be called a (9,5) scheme. Similarly, a (9,9) and a (5,9) scheme are obtained for $\mu = 0.5$ and $\mu = 1$ respectively. The HOC stencils emerging in this way have been illustrated in Figure 1.

The system of Equation (14) can be written in the matrix form as

$$A\boldsymbol{\Phi}^{\mathbf{n+1}} = \mathbf{f}(\boldsymbol{\Phi}^{\mathbf{n}}) \tag{15}$$

where the coefficient matrix A is an asymmetric sparse matrix. For a grid of size $m \times n$, A has a dimension mn, and $\boldsymbol{\Phi}^{\mathbf{n+1}}$ and $\mathbf{f}(\boldsymbol{\Phi}^{\mathbf{n}})$ are mn-component vectors. Partitioning A, $\boldsymbol{\Phi}^{\mathbf{n+1}}$ and $\mathbf{f}(\boldsymbol{\Phi}^{\mathbf{n}})$ into sub-matrices corresponding to the interior and boundaries, Equation (15) can be written as

$$\begin{pmatrix} A_L & 0 & 0 & 0 & 0 \\ 0 & A_B & 0 & 0 & 0 \\ 0 & 0 & A_D & 0 & 0 \\ 0 & 0 & 0 & A_T & 0 \\ 0 & 0 & 0 & 0 & A_R \end{pmatrix} \begin{pmatrix} \boldsymbol{\Phi}_{\mathbf{L}}^{\mathbf{n+1}} \\ \boldsymbol{\Phi}_{\mathbf{B}}^{\mathbf{n+1}} \\ \boldsymbol{\Phi}_{\mathbf{D}}^{\mathbf{n+1}} \\ \boldsymbol{\Phi}_{\mathbf{T}}^{\mathbf{n+1}} \\ \boldsymbol{\Phi}_{\mathbf{R}}^{\mathbf{n+1}} \end{pmatrix} = \begin{pmatrix} \mathbf{f}(\boldsymbol{\Phi}_{\mathbf{L}}^{\mathbf{n}}) \\ \mathbf{f}(\boldsymbol{\Phi}_{\mathbf{B}}^{\mathbf{n}}) \\ \mathbf{f}(\boldsymbol{\Phi}_{\mathbf{D}}^{\mathbf{n}}) \\ \mathbf{f}(\boldsymbol{\Phi}_{\mathbf{T}}^{\mathbf{n}}) \\ \mathbf{f}(\boldsymbol{\Phi}_{\mathbf{R}}^{\mathbf{n}}) \end{pmatrix}$$

where L, R, B and T stand respectively for the left, right, bottom and top boundaries of the domain and D for the interior. The block square matrices A_B and A_T are of order m, A_L and A_R are of order $(n-2)$, and A_D is of order $(m-2)(n-2)$. If boundary conditions are of Dirichlet type or they result in explicit expressions for the transport variables, the sub-matrices representing the boundary conditions are identity matrices. For an implicit expression, they will be sparse matrices with the number of non-zero entries in a particular row depending upon the order of the scheme. The matrix A_D has at most nine non-zero entries in each row. In matrix A, 0's are rectangular null matrices of orders ranging from $m \times (n-2)$ to $m \times (m-2)(n-2)$. The details of the elements of the column vectors on the left hand side

Copyright © 2002 John Wiley & Sons, Ltd.

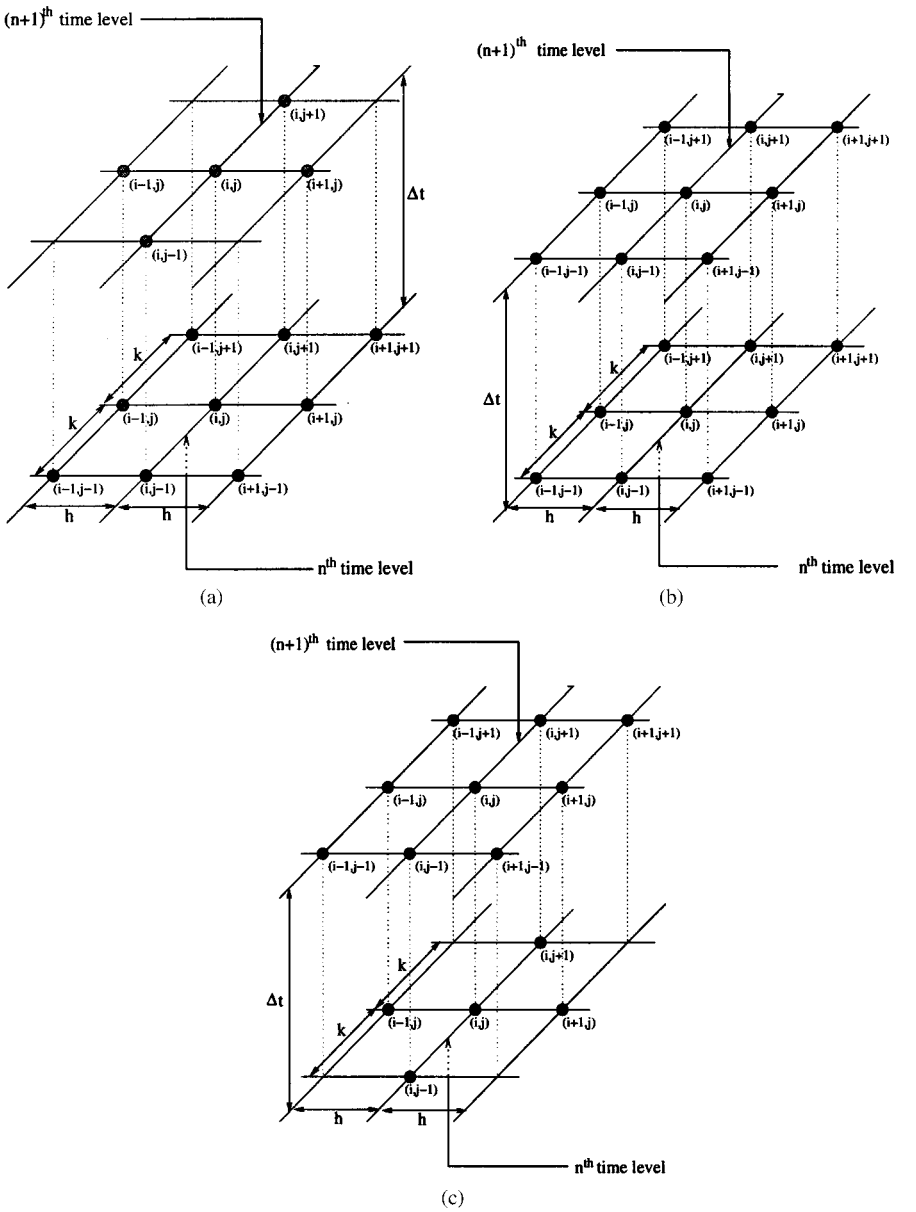

Figure 1. Unsteady HOC stencils for (a) $\mu = 0$, (b) $\mu = 0.5$ and (c) $\mu = 1.0$.

are as follows:

$$\mathbf{\Phi_L} = [\phi_{1,2}, \ldots, \phi_{1,n-1}]^\tau, \quad \mathbf{\Phi_B} = [\phi_{1,1}, \ldots, \phi_{m,1}]^\tau$$
$$\mathbf{\Phi_T} = [\phi_{1,n}, \ldots, \phi_{m,n}]^\tau, \quad \mathbf{\Phi_R} = [\phi_{m,2}, \ldots, \phi_{m,n-1}]^\tau$$

Copyright © 2002 John Wiley & Sons, Ltd.

and

$$\mathbf{\Phi_D} = [\phi_{2,2}, \ldots, \phi_{m-1,2}, \phi_{2,3}, \ldots, \phi_{m-1,3}, \ldots, \phi_{2,n-1}, \ldots, \phi_{m-1,n-1}]^{\tau}$$

On the right hand side, the $(n-2)$-component vectors $\mathbf{f}(\mathbf{\Phi_L^n})$ and $\mathbf{f}(\mathbf{\Phi_R^n})$, and the m-component vectors $\mathbf{f}(\mathbf{\Phi_B^n})$ and $\mathbf{f}(\mathbf{\Phi_T^n})$ correspond to the boundaries and the entries of the $(m-2)(n-2)$-component vector $\mathbf{f}(\mathbf{\Phi_D^n})$ are given at the right hand side of Equation (14). Thus $\mathbf{f}(\mathbf{\Phi^n})$ being known in terms of the current transport variables, Equation (15) can be solved with an iterative method for the transport variables in the next time level. The coefficient matrix arising from the present HOC discretization is not diagonally dominant and conventional iterative methods such as Gauss–Seidel cannot be used. Hence to solve the system of Equation (15), conjugate gradient method (**CG**) [19] for pure diffusion (when $c = d = 0$) and a hybrid biconjugate gradient stabilized method (**BiCGStab**) [20] for convection–diffusion have been employed without any pre-conditioning. For a problem having Dirichlet or explicitly expressed boundary conditions, A will have at most $2 \times (m+n-2) + 9 \times (m-2)(n-2)$ non-zero entries. Consequently, the matrix-vector product $A\mathbf{\Phi^{n+1}}$ required by the iterative solvers involves $2 \times (m+n-2) + 81 \times (m-2)(n-2)$ arithmetic operations only.

3. STABILITY ANALYSIS

A von Neumann linear stability analysis of the schemes is now performed assuming the convective coefficients c and d to be constants and forcing function g in Equation (1) to be zero for a particular HOC stencil with the (i,j)th node at the centre. If $\phi_{ij}^n = b^n e^{I\theta_x i} e^{I\theta_y j}$, where $I = \sqrt{-1}$, b^n is the amplitude at time level n, and $\theta_x (= 2\pi h/\Lambda_1)$ and $\theta_y (= 2\pi k/\Lambda_2)$ are phase angles with wavelengths Λ_1 and Λ_2 respectively, the amplification factor $\xi (= [(b^{n+1})/(b^n)])$, for stability, has to satisfy the relation

$$|\xi|^2 - 1 \leqslant 0$$

Now ξ can be found by substituting the expression for ϕ_{ij}^n and ϕ_{ij}^{n+1} in Equation (14) and the stability criterion of the schemes becomes

$$(1 - 2\mu) \leqslant \frac{2a}{\lambda_1(8 + h^2c^2) + \lambda_2(8 + k^2d^2)} \tag{16}$$

Introducing Courant numbers $C_x = c\Delta t/ah$, $C_y = d\Delta t/ak$ and cell Reynolds numbers $Re_h = ch$, $Re_k = dk$, we obtain

$$(1 - 2\mu)[C_x Re_h^{-1}(8 + Re_h^2) + C_y Re_k^{-1}(8 + Re_k^2)] \leqslant 2 \tag{17}$$

In particular, if $Re_h = Re_k = Re_c$ and $C_x = C_y = C$, then

$$C(1 - 2\mu) \leqslant \frac{Re_c}{8 + Re_c^2} \tag{18}$$

It is seen that a scheme is conditionally stable for $0 \leqslant \mu < 0.5$. The region of stability for this particular case represented by Equation (18) together with that of other schemes, viz. upwind, FTCS, and (9,9) scheme of Reference [13] are shown in Figure 2. Here, a scheme is stable in

Copyright © 2002 John Wiley & Sons, Ltd.

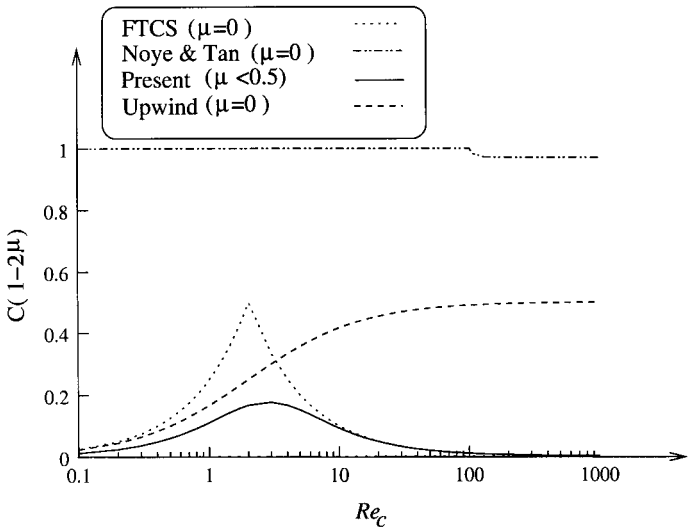

Figure 2. The regions of von Neumann stability for different schemes.

the region below its curve. Though the conditional stability criterion is restrictive particularly for large Re_c, for $0.5 \leqslant \mu \leqslant 1$, the scheme is unconditionally stable for all values of Re_c.

4. NUMERICAL TEST CASES

In order to study the validity and effectiveness of the proposed schemes, they are applied to one steady and three unsteady 2-D test problems. The unsteady problems are (i) the convection–diffusion of a Gaussian pulse, (ii) the flow decayed by viscosity and (iii) the Taylor's vortex problem, whereas the steady one is (iv) the lid-driven cavity flow. As the first three problems have analytical solutions, Dirichlet boundary conditions are used for them, whereas for the other one, both Dirichlet and Neumann boundary conditions are applied. All the computations are carried out on a HP 9000/C 200 computer.

4.1. Problem 1

Consider Equation (1) with $g = 0$ and constant convective coefficients in the square $0 \leqslant x,\ y \leqslant 2$ with initial condition given, as in Reference [14], by

$$\phi(x, y, 0) = \exp[-a((x - 0.5)^2 + (y - 0.5)^2)] \tag{19}$$

An analytical solution to this problem is

$$\phi(x, y, t) = \frac{1}{4t + 1} \exp\left[-\frac{a}{4t + 1}((x - ct - 0.5)^2 + (y - dt - 0.5)^2)\right] \tag{20}$$

The initial condition is a Gaussian pulse centred at $(0.5, 0.5)$ with pulse height 1. The boundary conditions have been taken from the analytical solution given by Equation (20). For the sake of comparison of our results with those of Reference [13], we choose $a = 100$ and $c = d = 80$.

Copyright © 2002 John Wiley & Sons, Ltd.

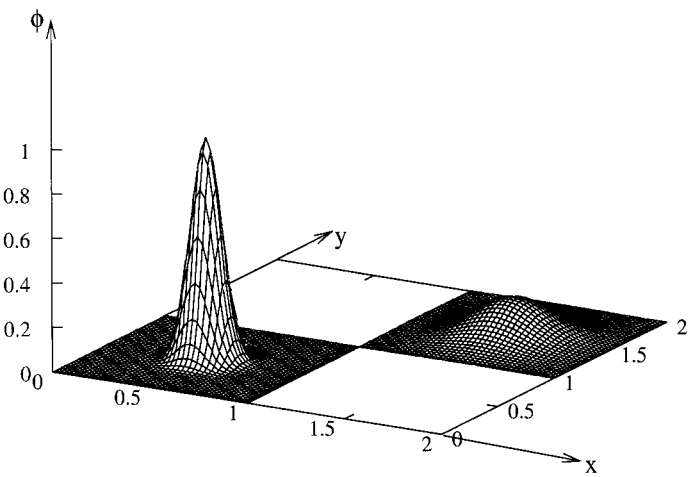

Figure 3. The initial and the numerical pulse at $t = 1.25$ $[(9,9), \Delta t = 0.00625]$.

The initial pulse and the pulse at $t = 1.25$ found through the present (9,9) scheme are shown in Figure 3. A remarkably similar picture is obtained from the analytical solution (Figure 4) where at $t = 1.25$ the Gaussian pulse moves to a position centred at $(1.5, 1.5)$ with a pulse height of $1/6$.

The average and the maximum absolute errors of different schemes including the present ones along with their CPU times have been presented in Table I. Using the modified equivalent partial differential equation (MEPDE) approach [13], it is found that if the time step is not small enough, the present $(9,5)$ and $(5,9)$ schemes are not adequate to capture the original pulse. This fact is also reflected in Figures 5(a) and 6(a). Table II depicts, at $t = 1.25$, the pulse height for different schemes and time steps. At the same instant, the location of the centre of the pulse is $(1.5, 1.5)$, the same as that of the exact pulse, for all computations in Table II. As seen from the same table, and Figures 5(a) and 7(a), the first order time accurate (9,5) scheme shows a pulse height higher than the exact because of the presence of in-built numerical anti-diffusion. To be precise, as seen from Figure 5(a), the anti-diffusion is prominent along the diagonal parallel to $y = x$, whereas little change in diffusion is noticed along the diagonal parallel to $y = -x$. This asymmetry in diffusivity produces elliptic contours. On the other hand, the in-built numerical diffusion in the (5,9) scheme explains the lower pulse height seen from Table II, and Figures 6(a) and 7(a). From Figure 6(a), it is clear that there is additive numerical diffusion along $y = x$, whereas diffusion along $y = -x$ remains largely unaffected. Table II shows that the magnitudes of numerical diffusivity and anti-diffusivity decrease with the reduction in time step and with smaller values, highly accurate solutions can be obtained. This is illustrated by the computed contours of Figures 5(b) and 6(b), and the exact contours of Figure 7(a). The (9,9) scheme gives a remarkably accurate solution even with a relatively larger time step $\Delta t = 0.00625$, yielding a pulse which is almost indistinguishable from the exact one as seen from Table II and Figures 4 and 7. It will be worthwhile to compare the time-wise efficiency of the present (9,9) scheme with the (9,9) scheme of Noye and Tan [13] as both the schemes are implicit and second order accurate in time. The CPU time ratio of the latter scheme to FTCS scheme is approximately 447 (30851:69) [13] whereas the same

Copyright © 2002 John Wiley & Sons, Ltd.

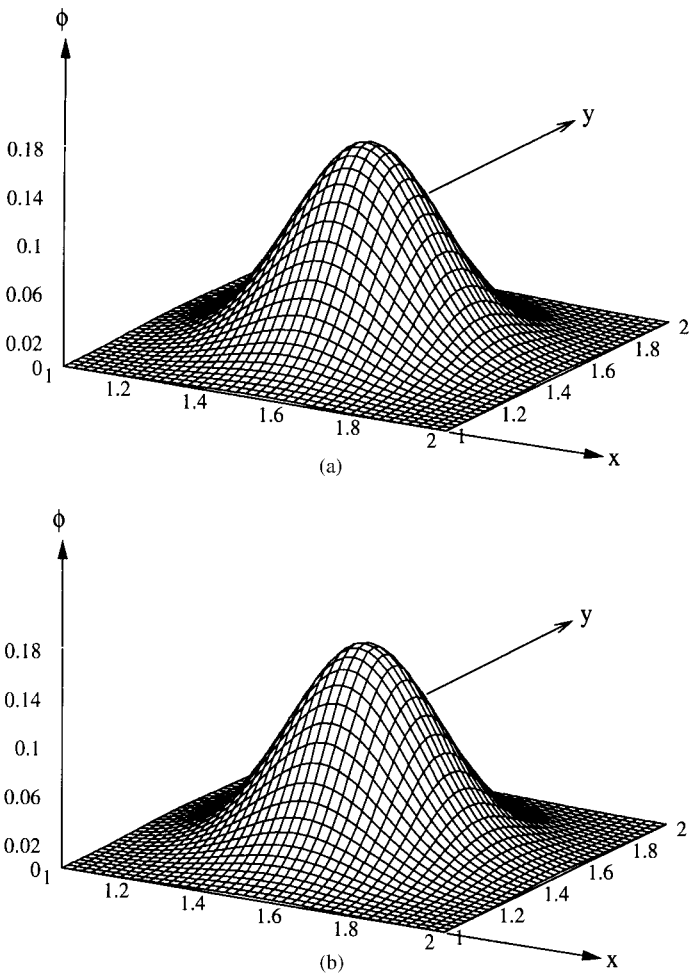

Figure 4. Surface plots of (a) exact and (b) numerical $[(9,9), \Delta t = 0.00625]$ pulse in the subregion $1 \leqslant x,\ y \leqslant 2$ at $t = 1.25$.

Table I. Error and CPU time for Problem 1 at $t = 1.25$ with $\Delta t = 0.0125$ and $h = k = 0.025$.

Method	Average|error|	Maximum|error|	CPU time (s)
FTCS	3.94×10^{-3}	1.21×10^{-1}	1.67
Upwind	2.65×10^{-3}	6.63×10^{-2}	3.34
Noye and Tan	1.43×10^{-5}	4.84×10^{-4}	—
Present (9,5)	1.49×10^{-3}	3.74×10^{-2}	16.34
Present (5,9)	1.02×10^{-3}	2.25×10^{-2}	11.74
Present (9,9)	1.59×10^{-5}	4.48×10^{-4}	8.78

Copyright © 2002 John Wiley & Sons, Ltd.

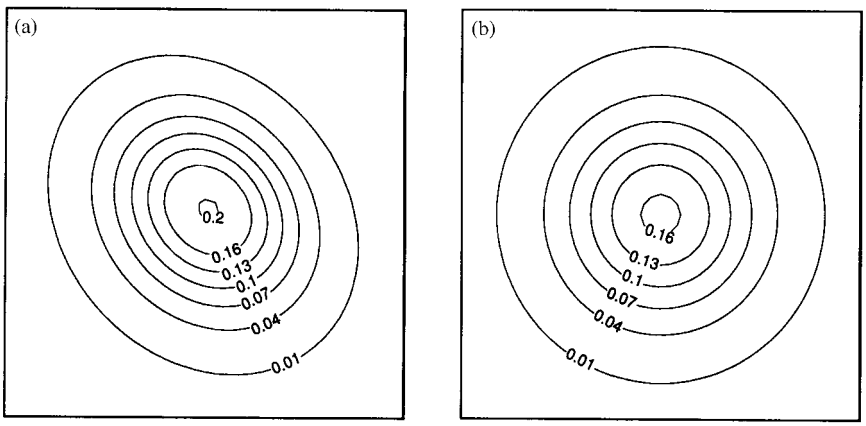

Figure 5. Contour plots of the pulse in the subregion $1 \leqslant x,\ y \leqslant 2$ at $t = 1.25$ for (9,5) scheme with (a) $\Delta t = 0.00625$ and (b) $\Delta t = 0.0001$.

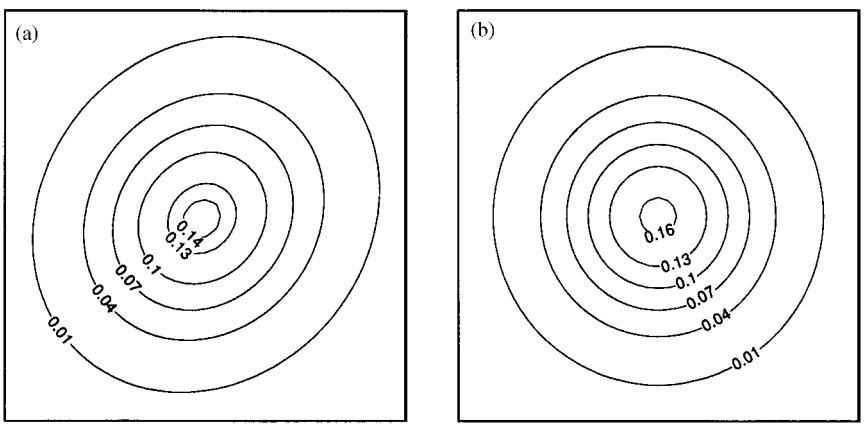

Figure 6. Contour plots of the pulse in the subregion $1 \leqslant x,\ y \leqslant 2$ at $t = 1.25$ for (5,9) scheme with (a) $\Delta t = 0.00625$ and (b) $\Delta t = 0.0001$.

for the present (9,9) scheme to FTCS is 5.257 (Table I). This clearly shows the superior time-wise efficiency of the present scheme.

In the next three examples, the results obtained only through the (9,9) scheme are presented, although sufficiently accurate results are obtained using the other two schemes as well.

4.2. Problem 2

The problem of flow decayed by viscosity [15, 16, 21] is governed by the 2-D N–S equations, which in non-dimensional form for an incompressible flow can be written as

$$\frac{\partial u}{\partial x} + \frac{\partial v}{\partial y} = 0 \tag{21}$$

Copyright © 2002 John Wiley & Sons, Ltd.

Table II. The pulse height at $t = 1.25$ with different time steps.

Method	Δt	Pulse height
(9,5)	0.00625	0.202492
	0.00025	0.167553
	0.0001	0.166852
(5,9)	0.00625	0.144447
	0.0001	0.165983
	0.00005	0.166210
(9,9)	0.0125	0.166863
	0.00625	0.166540
	0.0001	0.166656
Analytical		0.166667

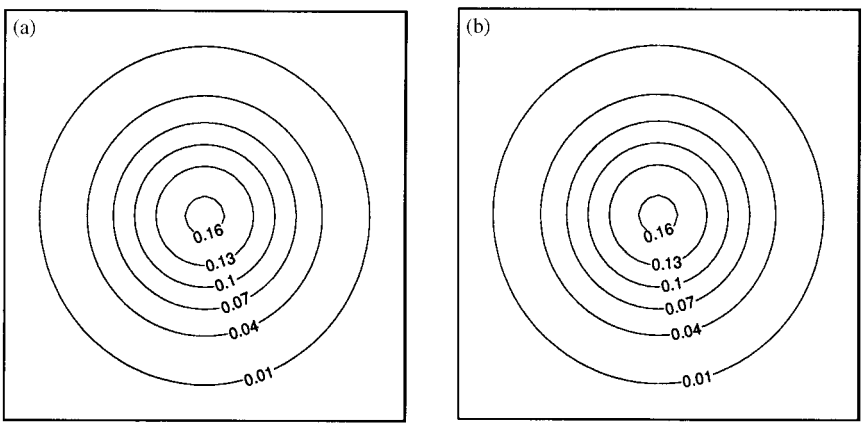

Figure 7. Contour plots of the pulse in the subregion $1 \leqslant x,\ y \leqslant 2$ at $t = 1.25$, (a) exact and (b) (9,9) scheme with $\Delta t = 0.00625$.

$$\frac{\partial u}{\partial t} + u\frac{\partial u}{\partial x} + v\frac{\partial u}{\partial y} = -\frac{\partial p}{\partial x} + \frac{1}{Re}\nabla^2 u \tag{22}$$

$$\frac{\partial v}{\partial t} + u\frac{\partial v}{\partial x} + v\frac{\partial v}{\partial y} = -\frac{\partial p}{\partial y} + \frac{1}{Re}\nabla^2 v \tag{23}$$

in the square $0 \leqslant x,\ y \leqslant \pi$. Here u and v are the velocities in the directions x and y, Re is the Reynolds number and, p is the pressure. The initial conditions are

$$u(x, y, 0) = -\cos x \sin y \quad \text{and} \quad v(x, y, 0) = \sin x \cos y \tag{24}$$

and boundary conditions at $x = 0$, $x = \pi$, $y = 0$ and $y = \pi$ are given by the following relations

$$u = -\cos x \sin y\, e^{-2t/Re} \quad \text{and} \quad v = \sin x \cos y\, e^{-2t/Re} \tag{25}$$

Copyright © 2002 John Wiley & Sons, Ltd.

Table III. Numerical and exact values of u and v at $(\pi/4, \pi/10)$ at different time levels, Re and grid sizes with $\Delta t = 0.01$ (Problem 2).

	u			v		
	Grid		Exact	Grid		Exact
	21×21	41×41		21×21	41×41	
			$Re = 50$			
$t = 0.1$	−0.217643	−0.217636	−0.217636	0.669812	0.669814	0.669814
$t = 0.5$	−0.214222	−0.214184	−0.214181	0.659179	0.659182	0.659182
$t = 1.0$	−0.210011	−0.209945	−0.209940	0.646122	0.646129	0.646129
			$Re = 100$			
$t = 0.1$	−0.218086	−0.218072	−0.218071	0.671153	0.671155	0.671155
$t = 0.5$	−0.216417	−0.216339	−0.216334	0.665802	0.665807	0.665807
$t = 1.0$	−0.214328	−0.214191	−0.214181	0.659168	0.659181	0.659182
			$Re = 1000$			
$t = 0.1$	−0.218523	−0.218473	−0.218464	0.672376	0.672364	0.672364
$t = 1.0$	−0.218684	−0.218155	−0.218071	0.671153	0.671154	0.671155
$t = 5.0$	−0.216842	−0.216435	−0.216334	0.665801	0.665807	0.665807
			$Re = 10\,000$			
$t = 0.1$	−0.218544	−0.218523	−0.218506	0.672511	0.672490	0.672485
$t = 1.0$	−0.219246	−0.218652	−0.218464	0.672383	0.672368	0.672364
$t = 5.0$	−0.218786	−0.218428	−0.218290	0.671832	0.671827	0.671826

The analytical solution to this problem is

$$u = -\cos x \sin y \, e^{-2t/Re}, \quad v = \sin x \cos y \, e^{-2t/Re} \quad \text{and} \quad p = -\frac{1}{4}(\cos 2x + \sin 2y) \, e^{-4t/Re} \tag{26}$$

Introducing stream-function ψ and vorticity ω, Equations (21)–(23) can be rewritten as

$$\frac{\partial \omega}{\partial t} + u \frac{\partial \omega}{\partial x} + v \frac{\partial \omega}{\partial y} = \frac{1}{Re} \nabla^2 \omega \tag{27}$$

$$\nabla^2 \psi = -\omega \tag{28}$$

where the initial and boundary conditions for ψ and ω can be derived from Equations (24) and (25). The pressure when needed, is obtained by solving the pressure Poisson equation,

$$\nabla^2 p = 2\left(\frac{\partial u}{\partial y} \frac{\partial v}{\partial x} - \frac{\partial u}{\partial x} \frac{\partial v}{\partial y} \right) \tag{29}$$

derived from Equations (21)–(23).

Results for different time steps and grid sizes are shown in Table III; it shows the computed values of u and v for four Reynolds numbers, viz. 50, 100, 1000 and 10 000 at different time levels at point $(\pi/4, \pi/10)$ together with the exact solutions. Obviously, grid independence is achieved with a grid as coarse as 21×21. Figure 8 shows the pressure contours obtained through the present scheme for $Re = 100$ at time $t = 0.1$ along with the exact contours. It is seen from these figures that the exact and numerical contours are almost indistinguishable.

Copyright © 2002 John Wiley & Sons, Ltd.

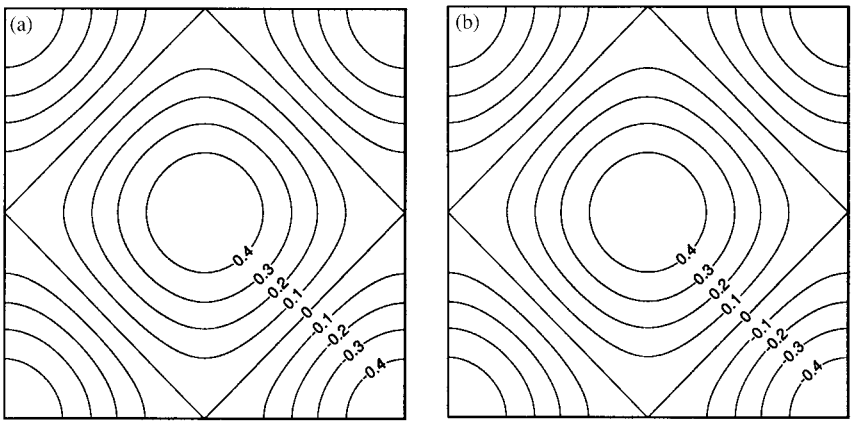

Figure 8. Pressure contours for $Re = 100$ at $t = 0.1$ for Problem 2, (a) numerical and (b) exact.

Strikwerda [15] mentioned that his higher order scheme is inadequate to provide realistic pictures of flows for Reynolds numbers beyond 100. However, present schemes are free from such limitations and highly accurate results are presented in Table III for a wide range of Reynolds numbers including a high $Re = 10\,000$.

4.3. Problem 3

In this example, the Taylor's vortex problem [16, 17] is considered with the following initial conditions

$$u(x, y, 0) = -\cos(Nx)\sin(Ny) \quad \text{and} \quad v(x, y, 0) = \sin(Nx)\cos(Ny) \quad \text{for } 0 \leqslant x, \ y \leqslant 2\pi \tag{30}$$

The exact solution of this problem is given by

$$u = -\cos(Nx)\sin(Ny)\, e^{-2N^2 t/Re} \quad \text{and} \quad v = \sin(Nx)\cos(Ny)\, e^{-2N^2 t/Re} \tag{31}$$

where N is an integer. Figure 9 depicts the computed Taylor's vorticity contours for $h = k = [(2\pi)/(64)]$, $Re = 1000$ and $N = 4$ at $t = 2$ with $\Delta t = 0.01$. The variations of the horizontal velocity along the vertical centerline and the vertical velocity along the horizontal centerline at time $t = 10$ and $Re = 100$ for $N = 1, 2$ and 4, along with the exact solutions are presented in Figure 10(a) and (b). Variations of the velocities on either sides of the axes exhibit identical behaviour with equal peak values. It is seen that our results are in good agreement with the exact solutions. The percentage error [16] of the maximum velocity (either u or v) has been used to test the accuracy of the schemes. For $Re = 20$ and $N = 1$ at time $t = 10$ on a 65×65 grid, this error for the (9,9) scheme is found to be 0.0071 per cent, which is much less than the minimum error 0.038 per cent obtained in Reference [17] with a 129×129 grid. For $N = 1, 2$ and 4, the percentage errors of the scheme are 0.054, 0.170 and 0.802 respectively for $Re = 1000$.

Copyright © 2002 John Wiley & Sons, Ltd.

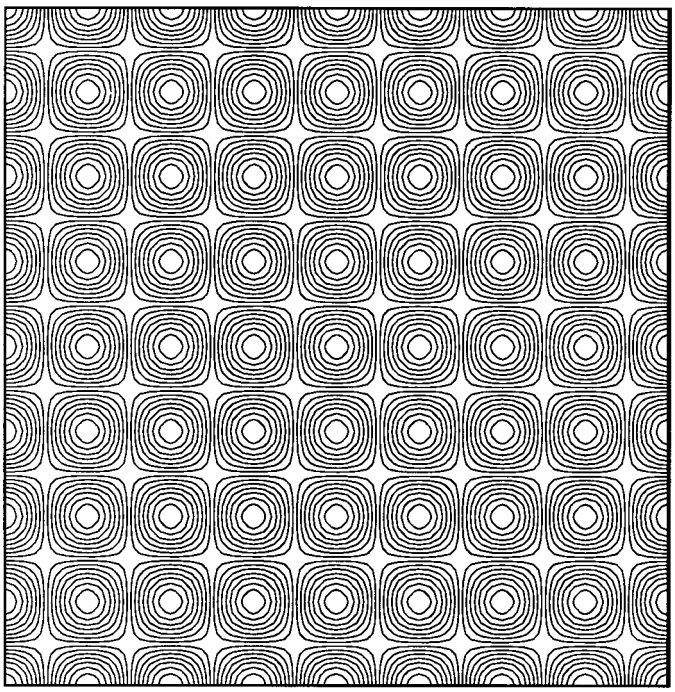

Figure 9. Vorticity contours for the Taylor's vortex at $t=2$ for $N=4$ and $Re=1000$ with $\Delta t=0.01$.

4.4. Problem 4

The problem considered here is the 2-D lid-driven cavity flow which is extensively used as a benchmark for code validation of the incompressible N–S equations. The cavity is defined by the square $0 \leqslant x,\ y \leqslant 1$. The governing equations are given by Equations (21)–(23). The top wall of the cavity at $y=1$ moving from left to right sets the fluid into motion. The velocities on that wall are $u=1$ and $v=0$, whereas on the other walls are $u=v=0$. The stream-function vorticity formulation have again been used here. A fourth order compact scheme for the Neumann boundary condition for vorticity has been used. For example, on the left wall, the approximation for ω can be found from the relation $v=-[(\partial\psi)/(\partial x)]$ and Equation (28) as

$$-\delta_x^+\psi_{0j}-\left[\frac{h}{2}+\frac{h^2}{6}\,\delta_x^+-\frac{h^3}{24}(Rev_{0j}\delta_y-\delta_y^2)\right]\omega_{0j}=v_{0j}-\frac{h^3}{24}(\delta_x^+\delta_y^2v_{0j}-\delta_t^+\omega_{0j}) \tag{32}$$

where the suffixes 0 and j stand for the left wall and the vertical index respectively. This results in an explicit expression for ω on the left wall. Vorticities on the other walls can be found in a similar way and for the corners, a third order scheme [6] has been used.

Computations are carried out using uniform grids of sizes 41×41, 81×81 and 121×121 with a time step $\Delta t=0.0125$ for $Re=100$ and 1000. Steady-state results are compared with those of Ghia *et al.* [22] and Spotz [23]. Table IV depicts the steady-state values ψ, ω and the location of the primary and the secondary bottom vortices along with their horizontal and

Copyright © 2002 John Wiley & Sons, Ltd.

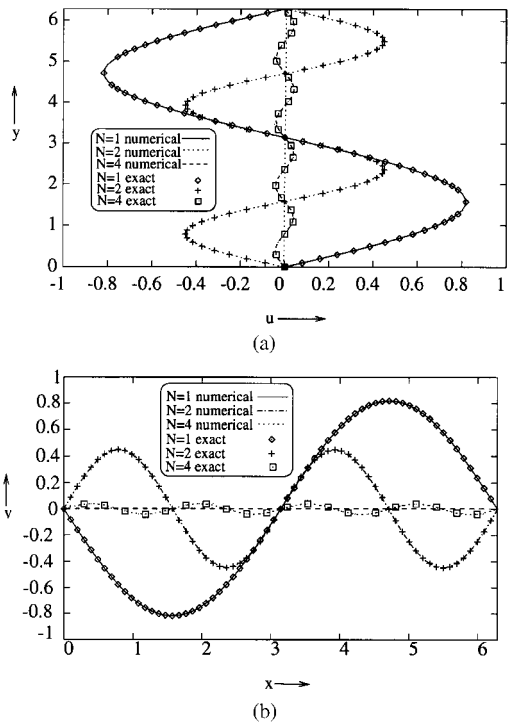

Figure 10. (a) Horizontal velocity along the vertical centerline and (b) vertical velocity along the horizontal centerline for the Taylor's vortex problem at $t = 10$ for $N = 1, 2$ and 4, and $Re = 100$.

Table IV. Steady-state vortex data for the lid-driven cavity problem for $Re = 1000$ ($\Delta t = 0.0125$).

Vortex	Method	ψ	ω	(x, y)	H_l	V_l
Primary	Present	−0.118750	−2.061801	(0.5333, 0.5750)	—	—
	Ghia	−0.117929	−2.04968	(0.5313, 0.5625)	—	—
	Spotz	−0.117240	−2.053332	(0.5250, 0.5750)	—	—
Bottom left	Present	0.000226	0.33275	(0.0833, 0.0750)	0.2156	0.1692
	Ghia	0.000231	0.36175	(0.0859, 0.0781)	0.2188	0.1680
	Spotz	0.000174	0.23915	(0.0750, 0.0750)	0.2189	0.1641
Bottom right	Present	0.001747	1.11624	(0.8667, 01167)	0.3023	0.3493
	Ghia	0.001751	1.15465	(0.8594, 0.1094)	0.3034	0.3536
	Spotz	0.001731	1.04409	(0.8750, 0.1250)	0.3067	0.3856

vertical lengths [(H_l) and (V_l)] for $Re = 1000$. Comparisons with the results of Reference [22] and the best results of Reference [23] show very good agreement. Figure 11(a) and (b) respectively compare the steady-state values of the horizontal velocity along the vertical centerline and vertical velocity along the horizontal centerline with the results of Reference [22]. Agreement in both the cases is excellent. Figures 12 and 13 show the steady-state

Copyright © 2002 John Wiley & Sons, Ltd.

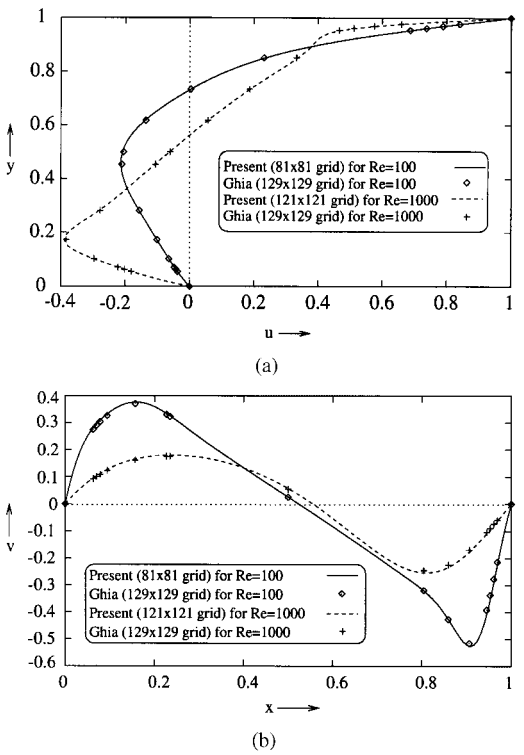

Figure 11. Steady-state results of the lid-driven cavity problem: (a) horizontal velocity along the vertical centreline and (b) vertical velocity along the horizontal centreline for $Re = 100$ and 1000.

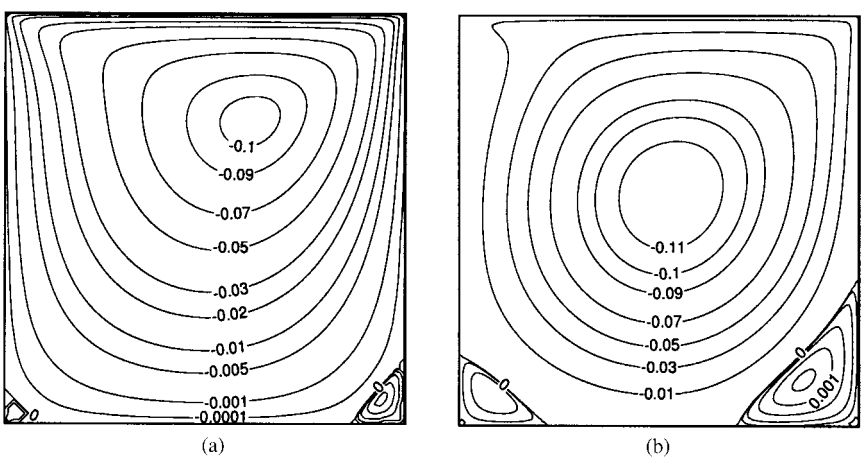

Figure 12. Steady-state stream function contours for the lid-driven cavity problem at (a) $Re = 100$ and (b) $Re = 1000$.

Copyright © 2002 John Wiley & Sons, Ltd.

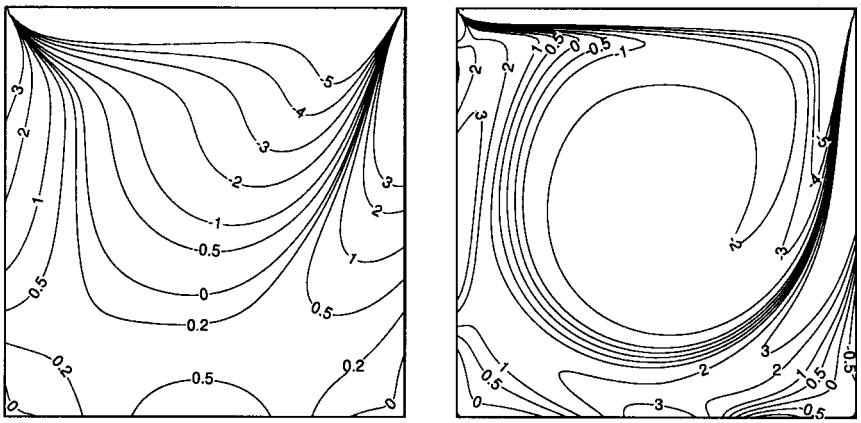

Figure 13. Steady-state vorticity contours for the lid-driven cavity problem at (a) $Re = 100$ and (b) $Re = 1000$.

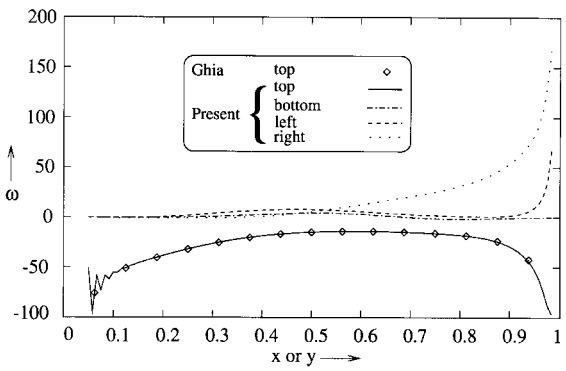

Figure 14. Steady-state vorticity on the four boundaries of the cavity for $Re = 1000$.

contours of stream-function and vorticity respectively for $Re = 100$ and 1000. It is seen from the figures that though the centre of the primary vortex is offset towards the top right corner for $Re = 100$, with increasing Re, it moves towards the geometric centre of the cavity (Figure 12). Also, as Re increases, several regions of high vorticity gradients, indicated by concentration of the vorticity contours, appear within the cavity (Figure 13). The steady-state vorticity distribution for $Re = 1000$ on the moving wall obtained by Ghia *et al.* [22] and on all the four walls obtained by the present (9,9) scheme are shown in Figure 14. In the case of the moving wall, there is some oscillation in the vorticity profile at the left end, as reported in Reference [6] for fourth order accurate boundary conditions. In general the solutions obtained through the present scheme, even on a coarser grid, are in excellent agreement with well-established results.

Copyright © 2002 John Wiley & Sons, Ltd.

5. CONCLUSION

A class of implicit HOC finite difference schemes has been developed with weighted time discretization to solve the unsteady 2-D variable coefficient convection–diffusion equation. Both Dirichlet and Neumann boundary conditions can easily be incorporated into the schemes. A linear stability analysis shows that the schemes are unconditionally stable for $0.5 \leqslant \mu \leqslant 1$. The schemes are second or lower order accurate in time according as $\mu = 0.5$ or otherwise, and fourth order accurate in space. In a departure from the rigidity of usual HOC schemes, the present schemes have been developed for a grid aspect ratio which need not necessarily be unity. Three schemes viz. (9,5), (9,9) and (5,9) for $\mu = 0, 0.5$ and 1 respectively have been investigated. They are easy to implement and the use of conjugate gradient and a hybrid biconjugate gradient stabilized algorithms for solving the algebraic systems arising at every time level, makes the implicit procedure computationally efficient even in capturing transient solutions. To bring out different aspects of the schemes, they have been employed to compute the transient solutions of three 2-D linear and nonlinear convection–diffusion problems and the time marching steady solution of the 2-D lid-driven cavity flow problem. The robustness of the schemes is illustrated by their applicability to the wide range of problems of varying physical complexities represented, among others, by Reynolds numbers ranging from 50 to 10 000. Computational efficiency of these schemes is reflected by the low demand on CPU time. This is substantiated by a comparison of the CPU time with an implicit scheme of identical temporal accuracy by Noye and Tan. The results obtained in all the four test cases with coarser grids are in excellent agreement with the analytical as well as established numerical results, underlining the high accuracy of the schemes. The implicit nature of the schemes is fully exploited in arriving at the steady-state results for the lid-driven cavity problem, where time-steps as high as 0.5 has been employed for some of the computations. Because of being HOC in space, second order accurate in time and implicit in nature, the (9,9) scheme in particular seems to have good potential for efficient application to many problems of incompressible viscous flows.

REFERENCES

1. Anderson DA, Tannehil JC, Pletcher RH. *Computational Fluid Mechanics and Heat Transfer*. Hemisphere Publishing Corporation: New York, 1984.
2. Anderson Jr JD. *Computational Fluid Dynamics*. McGraw-Hill, Inc.: New York, 1995.
3. Smith GD. *Numerical Solution of Partial Differential Equations: Finite Difference Methods*. Clarendon Press: Oxford, 1984.
4. Mackinnon RJ, Carey GF. Analysis of material interface discontinuities and superconvergent fluxes in finite difference theory. *Journal of Computational Physics* 1988; **75**(1):151–167.
5. Mackinnon RJ, Johnson RW. Differential equation based representation of truncation errors for accurate numerical simulation. *International Journal for Numerical Methods in Fluids* 199l; **13**:739–757.
6. Spotz WF, Carey GF. High-order compact scheme for the steady stream-function vorticity equations. *International Journal for Numerical Methods in Engineering* 1995; **38**:3497–3512.
7. Hirsh RS. Higher order accurate solution of fluid mechanics problems by a compact differencing technique. *Journal of Computational Physics* 1975; **9**:90–109.
8. Rai MM, Moin P. Direct simulations of turbulent flow using finite difference schemes. *Journal of Computational Physics* 1991; **96**:15–53.
9. Lele SK. Compact finite difference schemes with spectral like resolution. *Journal of Computational Physics* 1992: **103**:16–42.
10. Abarbanel S, Kumar A. Compact higher-order schemes for the Euler equations. *Journal of Scientific Computing* 1988; **3**:275–288.

Copyright © 2002 John Wiley & Sons, Ltd.

11. Balzano A. MOSQUITO: An efficient finite difference scheme for numerical simulation of 2D advection. *International Journal for Numerical Methods in Fluids* 1999; **31**:481–496.
12. Noye BJ, Tan HH. A third order semi implicit method for solving the one-dimensional convection–diffusion equation. *International Journal for Numerical Methods in Engineering* 1988; **26**:1615–1629.
13. Noye BJ, Tan HH. Finite difference methods for solving two-dimensional advection diffusion equation. *International Journal for Numerical Methods in Fluids* 1989; **9**:75–98.
14. Spotz WF. High order compact finite difference schemes for computational mechanics. *PhD thesis*, University of Texas at Austin, December, 1995.
15. Strikwerda JC. High-order accurate schemes for incompressible viscous flow. *International Journal for Numerical Methods in Fluids* 1997; **24**:715–734.
16. Yanwen M, Dexun F, Kobayashi T, Taniguchi N. Numerical solution of the incompressible Navier–Stokes equations with an upwind compact difference scheme. *International Journal for Numerical Methods in Fluids* 1999; **30**:509–521.
17. Chen Y, Yang S, Yang J. Implicit weighted essentially non-oscillatory schemes for the incompressible Navier–Stokes equations. *International Journal for Numerical Methods in Fluids* 1999; **31**:747–765.
18. Bodenmann R, Schroll HJ. Higher order discretization of initial boundary value problems for mixed systems. In *Proceedings Seminar für Angewandte Mathematik, ETH-Zurick*, number 96-05, May 1996.
19. Kelley CT. *Iterative Methods for Linear and Nonlinear Equations*. SIAM Publications: Philadelphia, 1995.
20. Sleijpen GLG, van der Vorst HA. Hybrid bi-conjugate gradient methods for CFD problems. *Computational Fluid Dynamics Review* 1995; 457–476.
21. Chorin AJ. Numerical solution of the Navier–Stokes equation. *Mathematics of Computation* 1968; **22**:747–762.
22. Ghia U, Ghia KN, Shin CT. High-Re solutions for incompressible flow using the Navier–Stokes equation and a multigrid method. *Journal of Computational Physics* 1982; **48**:387–411.
23. Spotz WF. Accuracy and performance of numerical wall boundary conditions for the 2D incompressible stream-function vorticity. *International Journal for Numerical Methods in Fluids* 1998; **28**:737–757.

Copyright © 2002 John Wiley & Sons, Ltd.